

Electronically driven spin-reorientation transition of the correlated polar metal $\text{Ca}_3\text{Ru}_2\text{O}_7$

Igor Marković^{a,b}, Matthew D. Watson^a, Oliver J. Clark^a, Federico Mazzola^a, Edgar Abarca Morales^{b,a}, Chris A. Hooley^a, Helge Rosner^b, Craig M. Polley^c, Thiagarajan Balasubramanian^c, Saumya Mukherjee^d, Naoki Kikugawa^e, Dmitry A. Sokolov^b, Andrew P. Mackenzie^{b,a}, and Phil D. C. King^{a,1}

^aSUPA, School of Physics and Astronomy, University of St Andrews, St Andrews KY16 9SS, United Kingdom; ^bMax Planck Institute for Chemical Physics of Solids, Nöthnitzer Straße 40, 01187 Dresden, Germany; ^cMAX IV Laboratory, Lund University, P. O. Box 118, 221 00 Lund, Sweden; ^dDiamond Light Source, Harwell Campus, Didcot, OX11 0DE, United Kingdom; ^eNational Institute for Materials Science, Tsukuba, Ibaraki 305-0003, Japan

This manuscript was compiled on May 26, 2020

The interplay between spin-orbit coupling and structural inversion symmetry breaking in solids has generated much interest due to the non-trivial spin and magnetic textures which can result. Such studies are typically focussed on systems where large atomic number elements lead to strong spin-orbit coupling, in turn rendering electronic correlations weak. In contrast, here we investigate the temperature-dependent electronic structure of $\text{Ca}_3\text{Ru}_2\text{O}_7$, a 4d oxide metal for which both correlations and spin-orbit coupling are pronounced, and in which octahedral tilts and rotations combine to mediate both global and local inversion symmetry-breaking polar distortions. Our angle-resolved photoemission measurements reveal the destruction of a large hole-like Fermi surface upon cooling through a coupled structural and spin-reorientation transition at 48 K, accompanied by a sudden onset of quasiparticle coherence. We demonstrate how these result from band hybridisation mediated by a hidden Rashba-type spin-orbit coupling. This is enabled by the bulk structural distortions and unlocked when the spin reorients perpendicular to the local symmetry-breaking potential at the Ru sites. We argue that the electronic energy gain associated with the band hybridisation is actually the key driver for the phase transition, reflecting a delicate interplay between spin-orbit coupling and strong electronic correlations, and revealing a new route to control magnetic ordering in solids.

ruthenate | magnetism | correlated oxide | Rashba spin-orbit | angle-resolved photoemission

Polar distortions in solids give rise to the well-known functionality of switchable macroscopic polarisation in ferroelectrics^(1,2) and, when combined with strong spin-orbit coupling, can mediate giant spin splittings of electronic states^(3,4). While typically found in insulators, ferroelectric-like distortions can remain robust against increasing itineracy, giving rise to so-called “polar metals”^(5–10). $\text{Ca}_3\text{Ru}_2\text{O}_7$ is the bilayer member of the $\text{Ca}_{n+1}\text{Ru}_n\text{O}_{3n+1}$ Ruddlesden-Popper series. The small ionic size of Ca induces large coupled rotations and tilts of the RuO_6 octahedra that make up the perovskite-like building blocks of this structure, generating a non-centrosymmetric crystal structure (space group #36: $Bb2_1m$, see Fig. 1(a))^(11,12). A symmetry-allowed trilinear coupling between the two non-polar octahedral tilt (X_3^-) and rotation (X_2^+) modes and a polar lattice mode (Γ_5^-) further mediates polar distortions, just as in $\text{Ca}_3\text{Ti}_2\text{O}_7$ and $\text{Ca}_3\text{Mn}_2\text{O}_7$ which are part of the well-known class of improper ferroelectrics^(13–15). Unlike these sister compounds, however, $\text{Ca}_3\text{Ru}_2\text{O}_7$ is not an insulator. Its in-plane resistivity decreases upon cooling from room temperature, albeit with a linear temperature dependence indicative of a so-called “bad metal” state^(16,17).

At $T_N = 56$ K, the system undergoes a Néel ordering transition, where the spins align ferromagnetically within each bilayer, oriented

along the a -axis, and are antiferromagnetically coupled between bilayers^(18,19). At a second phase transition at $T_S = 48$ K, the spins reorient to lie parallel to the in-plane b -axis^(11,18,19). Simultaneously, an iso-structural transition leads to a squashing of the unit cell along the c -direction⁽¹¹⁾. The resistivity exhibits a sudden jump on cooling through T_S , but, although its absolute value remains relatively high ($\rho_{ab}(5\text{ K}) \approx 50\ \mu\Omega\text{cm}$), the in-plane resistivity recovers a metallic temperature-dependence to low temperature^(16,17). A rich non-collinear magnetic texture has been observed under the application of magnetic fields⁽²⁰⁾, pointing to an important role of spin-orbit coupling combined with the non-centrosymmetric crystal structure, while strong electronic correlations are expected to also play an important role in shaping the electronic and magnetic properties of this system (the single-layered sister compound Ca_2RuO_4 is a Mott insulator⁽²¹⁾).

$\text{Ca}_3\text{Ru}_2\text{O}_7$ thus stands as a particularly rich example of a correlated polar metal. Gaining a comprehensive understanding of its transport, magnetic, and electronic properties has, however, proved elusive to date. Here, we study its temperature-dependent electronic structure by angle-resolved photoemission (ARPES, see Methods). Our low-temperature measurements are shown in Fig. 1. Consistent with Refs.^(22,23), we find a significant spectral weight in the valence bands associated with the Ru t_{2g} orbitals, but almost vanishing spectral weight at the Fermi level (Fig. 1(b)). Nonetheless, sharp features

Significance Statement

Methods to stabilise and control magnetic ordering in solids are strongly desired for both fundamental studies and to realise new spintronic technologies. The orientation of ordered magnetic moments is typically set by details of the crystalline environment in which they reside. Here, we report the discovery of a new form of magnetic anisotropy, which is instead driven by a striking reconfiguration of the underlying fermiology of the system. We show for the oxide material $\text{Ca}_3\text{Ru}_2\text{O}_7$ how this arises from the interplay of spin-orbit coupling, local polar distortions of the crystal structure, and pronounced electronic correlations. Our findings suggest new materials design approaches for manipulating magnetic textures, and open pathways to creating large magnetoelectric-type couplings in solids.

The ARPES measurements were performed by I.M., M.D.W., O.J.C., F.M., E.A.M. and P.D.C.K. and analysed by I.M., I.M. and H.R. performed the density-functional theory calculations. N.K. and D.S. grew and characterised the samples. C.M.P., T.B., and S.M. maintained the experimental ARPES capabilities and provided experimental support. I.M., M.D.W., C.A.H., A.P.M. and P.D.C.K. led the interpretation of the results, with input and discussion from all co-authors. I.M. and P.D.C.K. wrote the manuscript with input and discussion from all co-authors, and were responsible for the overall project planning and direction.

The authors declare no conflict of interest.

¹To whom correspondence should be addressed. E-mail: philip.king@st-andrews.ac.uk

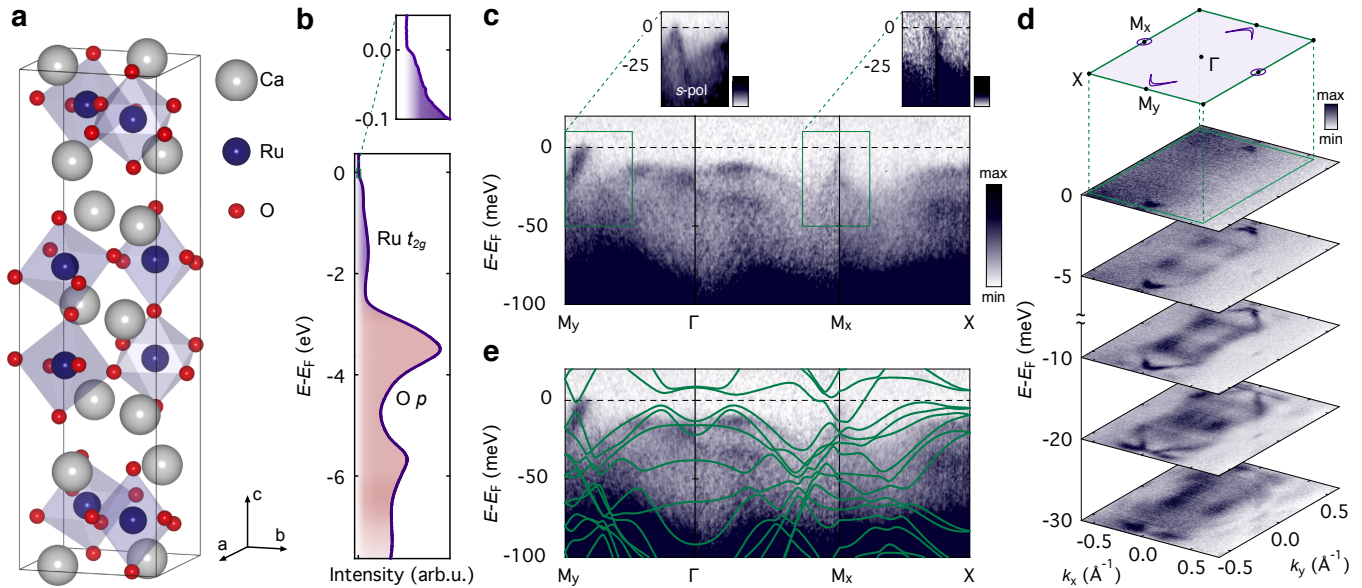


Fig. 1. Low-energy electronic structure of $\text{Ca}_3\text{Ru}_2\text{O}_7$. (a) Crystal structure of $\text{Ca}_3\text{Ru}_2\text{O}_7$. (b) Overview electronic structure measured at $T = 6$ K. A broad bandwidth associated with spectral weight from the Ru t_{2g} states is observed, while the spectral weight becomes very small close to the Fermi level. (c) Despite this, sharp quasiparticle-like states are observed at low energy. Close to M_y , a hole band just intersects the Fermi level, with both branches of the dispersion more clearly visible for measurements performed using s -polarised light (left inset; see SI Appendix, Fig. S1(b) for this data shown over an extended energy and momentum range). At M_x , an electron-like band crosses E_F , shown with enhanced contrast in the inset. (d) Constant energy contours measured at the Fermi level ($E_F \pm 2$ meV) and at finite binding energy. The Fermi surface is composed of tiny electron pockets located at the high-symmetry M_x point, and small boomerang-shaped hole Fermi surfaces located away from the Brillouin zone boundaries close to M_y . The inset shows the surface projected Brillouin zone of $\text{Ca}_3\text{Ru}_2\text{O}_7$ with schematics of the Fermi surfaces. Due to the weak spectral weight of the electron-like Fermi pockets, they are only just visible above the noise for the M_x point at $k_x > 0$, while their intensity is even further suppressed (likely by transition matrix element variations) for the pocket at $k_x < 0$. Additional states with ‘M-shaped’ dispersion are observed at slightly higher binding energy ((c), starting from $E - E_F \approx 10$ meV), which are also visible in constant energy contours below the Fermi level. (e) While the large unit cell and magnetic ordering give rise to a multitude of bands, we find that the general structure and form of the near- E_F states are well captured by ferromagnetic density-functional theory calculations (see Methods) when scaling the energy by a factor of 0.15.

are still evident on low energy-scales ($\lesssim 50$ meV, Fig. 1(c)), indicative of well-defined Fermi liquid-like quasiparticles, albeit with very low quasiparticle residue.

Our measured electronic structure exhibits a pronounced two-fold symmetry throughout the Brillouin zone. At the M_x point, an electron band intersects the Fermi level, giving rise to a small M_x -centred electron pocket (just visible in Fig. 1(d)). This derives from a band whose occupied bandwidth is only $\lesssim 15$ meV, immediately below which another band disperses downwards to higher binding energy (see right inset in Fig. 1(c)). The electronic structure is markedly different along the Γ - M_y direction. A dispersive state is evident intersecting the Fermi level away from the Brillouin zone boundary (Fig. 1(c)). An extremely weak feature is also visible with approximately the same k_F but opposite Fermi velocity (confirmed using measurements with different light polarisation, see left inset in Fig. 1(c)), indicating that this is the top of a Λ -shaped band which barely grazes the Fermi level. Fermi surface measurements (Fig. 1(d)) show how this disperses along the perpendicular in-plane direction to form a very narrow boomerang-shaped hole-like Fermi surface, centred along the Γ - M_y line but displaced away from the Brillouin zone boundary.

We thus assign the ground state of $\text{Ca}_3\text{Ru}_2\text{O}_7$ to be a low carrier-density compensated semi-metal, in agreement with the small Fermi pockets found previously by Shubnikov-de Haas studies⁽¹⁷⁾. An additional set of sharp and rather flat states are visible in Fig. 1(c,d) closer to the Brillouin zone centre. These bands display a shallow local minimum at Γ , disperse upwards towards their band maxima which are located ≈ 10 meV below the Fermi level⁽²²⁾, and then disperse back to higher binding energies, giving them a characteristic ‘M-shaped’ appearance. They are also visible as increased spectral weight close to

the Brillouin zone centre in constant energy maps for energies below the Fermi level in Fig. 1(d). Measurements using different light polarisations (SI Appendix, Fig. S1) indicate that there are at least 3 distinct states here, pointing to a rich multi-band near- E_F electronic structure. To further explore this, we show in Fig. 1(e) density-functional theory (DFT) calculations of the low-temperature electronic structure (see Methods), renormalised in energy by a factor of ≈ 7 .

The strong bandwidth renormalisation needed to achieve a reasonable agreement with the measured low-energy electronic structure indicates that $\text{Ca}_3\text{Ru}_2\text{O}_7$ is a highly correlated metal, consistent with its low quasiparticle residues. In such a complex multi-band system as this, momentum- and orbital-dependent self energies may generically be expected⁽²²⁾, and a simple bandwidth scaling cannot be expected to capture in detail the full influence of many-body interactions on the electronic structure. Indeed, the experimental Fermi velocities of the boomerang-shaped states crossing E_F are only renormalised by a factor of ≈ 4 as compared to corresponding features in the DFT, while the flat bands appear to require significantly higher renormalisations. The results shown here thus motivate future study of interaction effects in $\text{Ca}_3\text{Ru}_2\text{O}_7$ by state-of-the-art correlated electronic structure calculations, of the form that have recently proved extremely successful in describing the single-layer Sr-based sister compound^(24,25). Nonetheless, we note that a global bandwidth scaling of the calculated DFT still does a remarkably good job in reproducing the key experimental band structure features observed here, including the M_x -centred electron pocket, the hole-like Λ -band offset from the M_y point (located just below E_F in the calculations), and the fully-occupied ‘M-shaped’ states just below the Fermi level.

The marked difference in the calculated electronic structure along

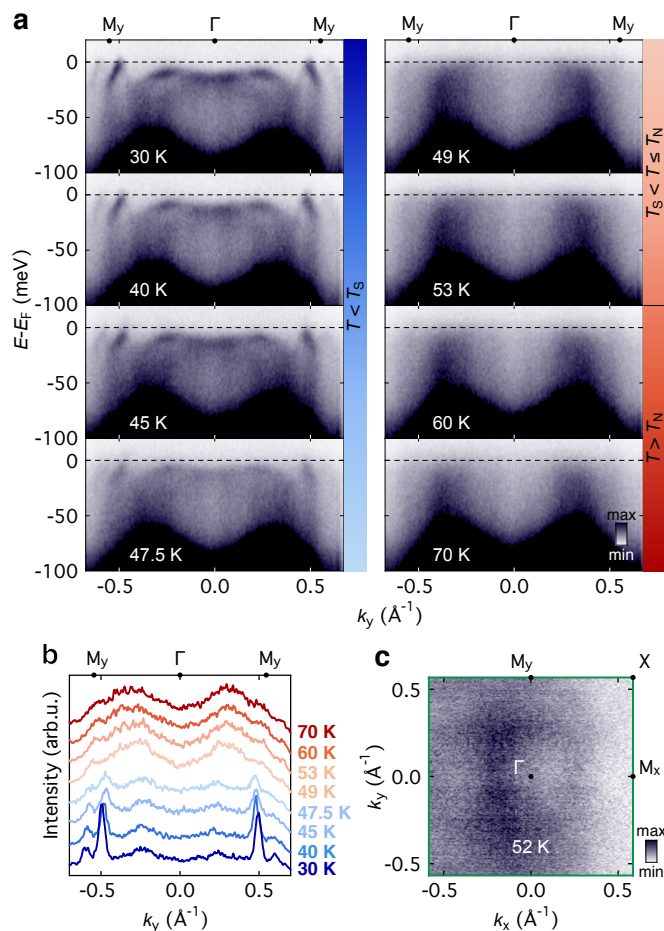


Fig. 2. Fermi surface transition at T_S . (a) Temperature-dependent ARPES dispersions (measured along the Γ - M_y direction) and (b) corresponding Fermi level momentum distribution curves (MDCs, $E_F \pm 2$ meV) indicate a gradual temperature-dependent increase in the quasiparticle linewidth with increasing temperature below the coupled structural and spin-reorientation transition at $T_S = 48$ K. Upon warming through this transition, a sudden and extreme spectral broadening is observed, pointing to a loss of quasiparticle coherence at the transition. The ‘M-shaped’ states at low temperature now disperse up through the Fermi level, forming (c) a large Fermi surface, but with a very high scattering rate. No qualitative changes are observed upon warming further through the Néel transition at $T_N = 56$ K (a).

the Γ - M_x and Γ - M_y directions demonstrates that the large anisotropy in the measured electronic structure along these directions can be fully explained on the basis of the orthorhombic crystal structure, without invoking an electronically driven nematicity as reported in a very recent study⁽²³⁾. Moreover, our calculations indicate that the flattened ‘M-shaped’ dispersion at the Brillouin zone centre, clearly evident in the experimental electronic structure in Fig. 1(c), is the result of a band hybridisation between the top of a hole-like band and the bottom of an electron-like band, with a gap opening at the Fermi level. We will show below that this band hybridisation is in fact key to understanding much of the important physics of $\text{Ca}_3\text{Ru}_2\text{O}_7$.

Fig. 2(a) shows the temperature-dependent evolution of the electronic structure through the two phase transitions. For temperatures below the structural and spin-reorientation transition, T_S , the spectral linewidths gradually broaden with increasing sample temperature (Fig. 2(b)), as can generically be expected from electron-electron and electron-phonon interactions. While $\text{Ca}_3\text{Ru}_2\text{O}_7$ is sometimes considered to be in an insulating state above $T \approx 30$ K, our spectroscopic measurements clearly demonstrate that well-defined quasiparticle-like

states persist up to T_S . In contrast, we find a sudden and dramatic loss of quasiparticle coherence when warming through T_S , with extremely broad linewidths above the transition indicative of a high scattering rate. The electronic structure is also markedly altered across the transition. While the transition at T_S is known to be first order^(16,26,27), the corresponding thermal hysteresis is small⁽²⁶⁾, and we do not observe it (or signatures of coexisting domains) within the temperature resolution of our experiments (~ 2 K). While weak and broad remnants of the original Fermi crossings still persist above T_S (evident as shoulders at $k_y \approx \pm 0.55 \text{ \AA}^{-1}$ in Fig. 2(b)), the state around the Brillouin zone centre now no longer appears to bend back to form an ‘M-shaped’ dispersion. Rather, it crosses directly through E_F , forming a large hole-like Fermi surface centred at Γ (Fig. 2(c)), consistent with a known transition in the Hall coefficient from large and negative values at low temperatures to small and positive values above T_S ^(28,29). We note in passing that this high temperature Fermi surface is two-fold rather than four-fold symmetric, again reflecting the large orthorhombicity of the lattice. The evident loss of quasiparticle coherence, despite the pronounced increase in carrier density, upon warming through T_S is interesting, and requires further detailed study. Qualitatively it may be related to the multi-band nature of $\text{Ca}_3\text{Ru}_2\text{O}_7$. The creation of new Fermi pockets, and the additional density of states associated with these, will open new channels for inter- and intra-band scattering. Moreover, there are a large number of bands with turning points expected in the vicinity of the Fermi level; recent work has emphasised the potential for strong scattering for all states in the Brillouin zone to be associated with the presence of hot spots localised in k -space⁽³⁰⁾. We note, however, that this is a complex system with both a structural and magnetic transition occurring here, and we do not exclude that additional contributions from electron-lattice and electron-magnon coupling could contribute to the changes observed experimentally.

We focus below on the origin of the unusual moment orientation-dependent Fermi surface transition at T_S . Our measurements indicate that once the large, zone-centred Fermi surface is established upon warming through T_S , the electronic structure evolves only gradually, with no further qualitative changes as the temperature is increased to above the 56 K Néel transition (Fig. 2(a,b)). Such an insensitivity to the antiferromagnetic ordering at T_N might naively suggest that it is the structural, rather than spin-reorientation, aspect of the phase transition at T_S which underpins the dramatic changes in electronic structure observed there. We show below, however, that this is in fact not the case.

Fig. 3 shows the electronic structure as calculated by DFT for the experimental crystal structures above and below the structural transition at T_S , and for the spin oriented along different in-plane crystallographic directions. For the spin moment oriented along the a -axis and for the 50 K crystal structure (Fig. 3(a), as found for $T_S < T \leq T_N$), the hybridisation of the electron- and hole-like bands at the Brillouin zone centre is evidently suppressed. This gives rise to the large Fermi surfaces observed experimentally around the Brillouin zone centre. A similar lack of band hybridisation of the near- E_F states is found when considering the equivalent spin configuration but for the low-temperature crystal structure (Fig. 3(b)), pointing to an insensitivity of the low-energy electronic structure to the structural component of the transition at T_S . In contrast, when the moment is rotated to lie along the b -axis (as found experimentally for $T < T_S$) the electron and hole bands at the zone centre develop a strong hybridisation. The hybridisation develops gradually as the moment is rotated away from the a -axis in both ab and ac planes (Fig. 3(d)). This demonstrates that it is the moment orientation and

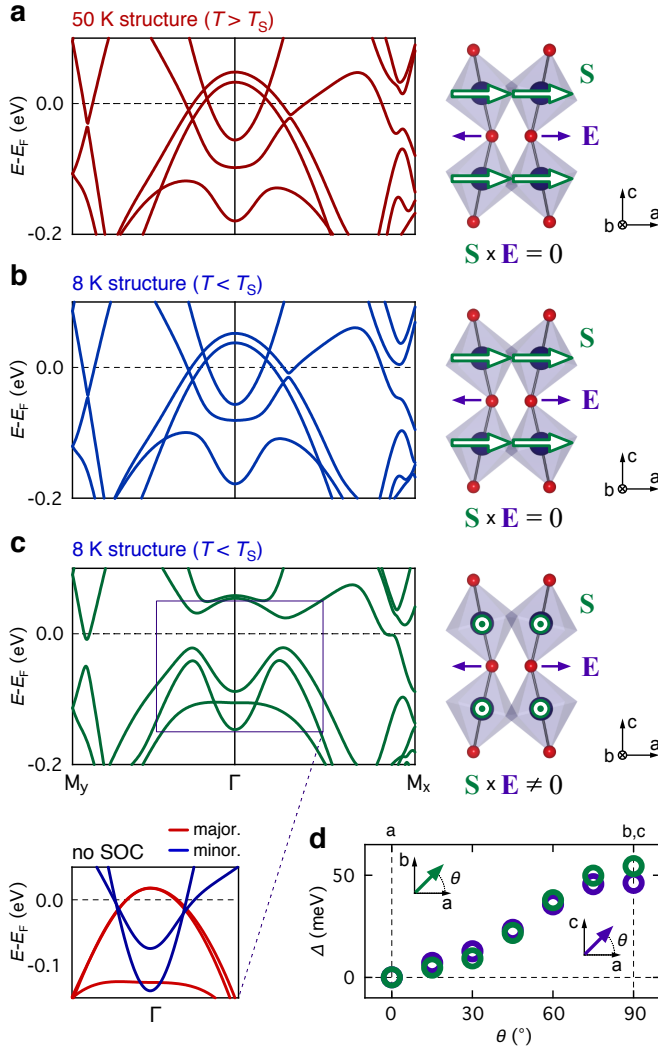


Fig. 3. Asymmetric spin-orbit driven band hybridisation. (a) Calculated electronic structure from density-functional theory for the experimental crystal structure at $T = 50$ K ($T > T_S$) and with the spin moments aligned along the in-plane a -axis, as observed experimentally for $T_S < T \leq T_N$. (b,c) Equivalent calculations for (b) the low-temperature crystal structure (for $T = 8$ K) with spin moments still oriented along the a -axis, and (c) the low-temperature crystal structure with spin moments along the b -axis, as observed experimentally for $T < T_S$. The schematics in (a-c) show representative views of the Ru sites in a RuO_2 bilayer, showing the tilt and resulting local polarisation (purple arrows) and the spin moment orientation (green arrows). The inset of (c) shows the corresponding electronic structure calculated without including spin-orbit coupling, indicating that the hybridisation gap which opens at the Fermi level is between spin majority-like (red) and minority-like (blue) $\text{Ru } t_{2g}$ states, and opens via spin-orbit coupling. (d) The magnitude of the hybridisation gap grows smoothly as the moment is rotated away from the a axis within both ab and ac (purple points) planes.

not the structural changes at T_S that mediate the opening of a band gap at the Fermi level observed here experimentally (Fig. 3(c) and Fig. 1(e)).

The relevant hybridised states at the Fermi level here derive from spin-minority-like and spin-majority-like $\text{Ru } t_{2g}$ -derived bands (Fig. 3(c, inset))⁽³¹⁾. The details of the low-energy DFT band structure are sensitive to the precise degree of exchange splitting, which varies with the choice of exchange-correlation functional and is larger when using a GGA functional than for an LDA one (see SI Appendix, Fig. S2 for a comparison). We find that the LDA calculation better describes the experimental data, with the large hole-like pocket

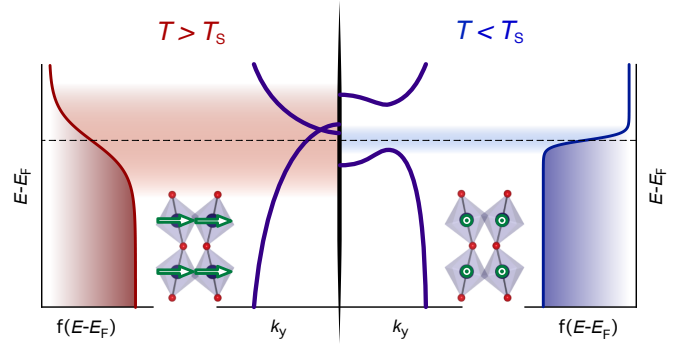


Fig. 4. Electronically driven magnetocrystalline anisotropy. Schematic representation of the renormalised electronic structure of the zone-centre states corresponding to (left) $T > T_S$ and (right) $T < T_S$. At high temperatures, the broad Fermi function leads to thermal population of the states that are pushed upwards by band hybridisation in the low-temperature case, removing any associated energy gain with hybridising these states. Upon cooling, this energy gain becomes active, ultimately driving the spin reorientation in order to enable the band hybridisation via Rashba-type spin-orbit coupling.

present at Γ , although the electron pocket there is not clearly seen in the dispersions measured above T_S (Fig. 2(a)), and the experimental situation may in fact be best reflected by an exchange splitting that is between the results of these two calculations. We stress, however, that both functionals show qualitatively the same behaviour (SI Appendix, Fig. S2), namely a hybridisation of zone-centre electron and hole-like bands below T_S . This hybridisation is mediated by spin-orbit coupling (Fig. 3(c)), with a gap that opens throughout the Brillouin zone (Fig. 1(d) cf. Fig. 2(c)) and develops gradually as the spin moment is rotated away from the a -axis (Fig. 3(d)), but is almost invariant when the moment is rotated between the b and c axes (SI Appendix, Fig. S3).

We attribute this spin moment-dependent gapping to a local breaking of inversion symmetry driven by the X_3^- tilt mode of the RuO_6 octahedra^(44,15). The vertically-stacked octahedra of the perovskite bilayer develop hinge-like distortions about the shared apical oxygen, which reverse in direction between neighbouring in-plane sites as shown schematically in Fig. 3. Each pair of outer apical oxygens are displaced in the opposite direction to the shared central apical oxygen. This leads to a local polarisation oriented along the tilt direction (the a -axis here) with an antiferro-type ordering within the ab plane. No net polarisation is generated along a . Locally, however, an asymmetric spin-orbit coupling of the Rashba-type⁽³²⁻³⁴⁾, $\mathcal{H}_R \propto \mathbf{p} \cdot (\mathbf{S} \times \mathbf{E})$, can generically be expected, where \mathbf{p} is the electron momentum, \mathbf{E} is an effective internal electric field along the a -axis representing the local inversion asymmetry, and \mathbf{S} is the electron spin of the itinerant states, which are fixed along one of the in-plane crystallographic axes by the magnetic moment orientation. This provides a natural explanation for the hybridisation of intra-bilayer spin-majority and minority bands observed here. For the spin moment aligned along the a -axis (Fig. 3(a,b), $\mathbf{S} \times \mathbf{E} = 0$), the Rashba-type term cannot act and thus no hybridisation would be expected from this form of spin-orbit coupling. In contrast, at the spin reorientation transition where the moment aligns along the b -axis (Fig. 3(c)), the Rashba-like spin-orbit interaction becomes active ($\mathbf{S} \times \mathbf{E} \neq 0$), enabling the band hybridisation.

When the hybridisation is allowed, the large hole-like Fermi surface thus becomes gapped. The corresponding hybridisation energy scale in our DFT calculations is on the order of 50 meV. In reality, however, the true hybridisation gap is renormalised to significantly

smaller values due to the strong electronic correlations of this system. We estimate that the true gap magnitude in the low-temperature phase is $\approx 10 - 15$ meV, comparable to a 13 meV gap (originally attributed to a pseudogap) which was seen to open in optical spectroscopy measurements upon cooling through T_S ⁽³⁵⁾. The gap size is thus comparable to thermal energy scales at T_S . We propose that at the Néel transition, the fluctuating moments of the paramagnetic state above T_N develop a long-range order, with the spin orientation fixed along the a -axis by conventional magnetocrystalline anisotropy effects. There is no electronic incentive for orienting the moment along b , as the hybridised states above E_F would be thermally populated (Fig. 4); the crystalline terms thus dominate. Upon further cooling, however, the thermal population effects are reduced. The electronic energy gain from the opening of a band gap at the Fermi level thus becomes sufficient to favour the spin reorientation such that local Rashba-type spin-orbit coupling can hybridise the relevant electronic states.

Our results thus suggest a Rashba-mediated band hybridisation of low-energy states ultimately leads to the first-order magnetic, and accompanying structural, phase transition in $\text{Ca}_3\text{Ru}_2\text{O}_7$. Our analysis has a number of important implications. It identifies a new source of magnetic anisotropy in metals, where the magnetic moment direction is set by an electronic energy gain from gapping much of the Fermi surface. In that sense it is a ‘magneto-electronic’ rather than a magnetocrystalline anisotropy. Materials where inversion symmetry is broken either within the host crystal structure, or by heterostructuring approaches^(9,13,36) and at surfaces and interfaces^(37,38), will provide interesting playgrounds in which to seek to stabilise such magneto-electronic anisotropy via asymmetric spin-orbit coupling as reported here. Other crystalline symmetries could in principle also be utilised, with the electronic energy gain being driven by spin moment reorientations that break the symmetries which otherwise protect specific band crossings in the vicinity of the Fermi level. Conversely, external switching of the moment orientation, for example via application of magnetic fields, would provide a novel route to control gapping of the Fermi surface states, and through this induce pronounced responses in the transport properties of multi-orbital correlated magnets such as $\text{Ca}_3\text{Ru}_2\text{O}_7$ studied here.

Materials and Methods

Single crystal growth: Single crystals of $\text{Ca}_3\text{Ru}_2\text{O}_7$ were grown using a floating zone method in a mirror furnace (Canon Machinery, model SCI-MDH)⁽³⁹⁾. The crystal growth was performed in an atmosphere of a mixture of Ar and O_2 (Ar : O_2 = 85 : 15). In general, antiphase domains can be expected, and are visible via contrast in polarised light optical microscopy (SI Appendix, Fig. S4). We used this to select samples which are single-domain over a scale of at least $500 \times 500 \mu\text{m}^2$. The mono-domain nature of our resulting samples is further evident in our measured Fermi surfaces, which show a clear two-fold symmetry with no signatures of rotated features coming from different domains.

Angle-resolved photoemission: ARPES measurements were performing using the BLOCH beamline of the Max-IV synchrotron and the I05 beamline of Diamond Light Source. Measurements were performed using p -polarised 22 eV synchrotron light. Additional data measured using s -polarised light is shown in SI Appendix, Fig. S1. The samples were cleaved *in situ*, and measured at temperatures between 6 K and 70 K, as specified in the figures. Temperature-dependent data sets were repeated on multiple samples and via both warming and re-cooling cycles, confirming that the changes shown in Fig. 2 are intrinsic and are not a result of sample ageing upon temperature cycling.

Density-functional theory: Density functional theory (DFT) calculations were performed using the Local Spin Density Approximation (LSDA) exchange-correlation functionals, as implemented in the full-potential FPLO code^(40–42). Additional calculations were performed with the Perdew-Burke-Ernzerhof (PBE) functional⁽⁴³⁾, and are shown and discussed in SI Appendix, Fig. S2. The experimental crystal structures were used in all cases⁽¹¹⁾, and spin-orbit coupling was included throughout. The Brillouin zone sampling employed a k -mesh of at least $16 \times 16 \times 6$ k -points. Additional calculations were performed using WIEN2K⁽⁴⁴⁾, and gave consistent results. We employed ferromagnetic calculations, neglecting the antiferromagnetic coupling between neighbouring bilayers. Given the ferromagnetic ordering within the bilayer and the weak coupling between bilayers, this does not affect any of the key conclusions drawn from our calculations, as confirmed by the broad agreement between our calculations and the experimentally measured electronic structure shown in Fig. 1(e).

Data deposition: The data that underpins the findings of this study are available from the University of St Andrews research portal, *doi to be inserted prior to publication*.

ACKNOWLEDGMENTS. We thank Erez Berg, Bernd Braunecker, Sean Hartnoll, Phil Lightfoot, Finlay Morrison, Roderich Moessner, Silvia Picozzi, Ulrich Röbber, Andreas Rost, and Veronika Sunko for useful discussions. We gratefully acknowledge support from the European Research Council (through the ERC-714193-QUESTDO project), the Royal Society, the UK Research and Innovation (via grant numbers EP/R031924/1 and EP/R025169/1), the Max-Planck Society, and the Japan Society for the Promotion of Science KAKENHI (Nos. JP17H06136 and JP18K04715) and Japan Science and Technology Agency JST-Mirai Program (No. JPMJMI18A3). IM and EAM acknowledge studentship support through the International Max-Planck Research School for the Chemistry and Physics of Quantum Materials. We thank Ulrike Nitzsche for technical support with the DFT calculations. We thank Diamond Light Source and Max-IV synchrotrons for access to Beamlines I05 (Proposal Nos. S121986 and S125040) and BLOCH (Proposal No. 20180399), respectively, that contributed to the results presented here.

References

- Rabe, K. M., Dawber, M., Lichtensteiger, C., Ahn, C. H. & Triscone, J.-M. Modern Physics of Ferroelectrics: Essential Background. In *Physics of Ferroelectrics*, vol. 105, 1–30 (Springer Berlin Heidelberg, Berlin, Heidelberg, 2007).
- Scott, J. F. Applications of Modern Ferroelectrics. *Science* **315**, 954–959 (2007).
- Di Sante, D., Barone, P., Bertacco, R. & Picozzi, S. Electric Control of the Giant Rashba Effect in Bulk GeTe. *Advanced Materials* **25**, 509–513 (2013).
- Picozzi, S. Ferroelectric Rashba semiconductors as a novel class of multifunctional materials. *Frontiers in Physics* **2** (2014).
- Anderson, P. W. & Blount, E. I. Symmetry Considerations on Martensitic Transformations: ‘Ferroelectric’ Metals? *Physical Review Letters* **14**, 217–219 (1965).
- Shi, Y. *et al.* A ferroelectric-like structural transition in a metal. *Nature Materials* **12**, 1024–1027 (2013).
- Puggioni, D. & Rondinelli, J. M. Designing a robustly metallic noncentrosymmetric ruthenate oxide with large thermopower anisotropy. *Nature Communications* **5**, 3432 (2014).
- Benedek, N. A. & Birol, T. ‘Ferroelectric’ metals reexamined: fundamental mechanisms and design considerations for new materials. *Journal of Materials Chemistry C* **4**, 4000–4015 (2016).
- Kim, T. H. *et al.* Polar metals by geometric design. *Nature* **533**, 68–72 (2016).
- Laurita, N. J. *et al.* Evidence for the weakly coupled electron mechanism in an Anderson-Blount polar metal. *Nature Communications* **10**, 3217 (2019).
- Yoshida, Y. *et al.* Crystal and magnetic structure of $\text{Ca}_3\text{Ru}_2\text{O}_7$. *Physical Review B* **72**, 054412 (2005).
- Lei, S. *et al.* Observation of Quasi-Two-Dimensional Polar Domains and Ferroelastic Switching in a Metal, $\text{Ca}_3\text{Ru}_2\text{O}_7$. *Nano Letters* **18**, 3088–3095 (2018).
- Bousquet, E. *et al.* Improper ferroelectricity in perovskite oxide artificial superlattices. *Nature* **452**, 732–736 (2008).
- Benedek, N. A. & Fennie, C. J. Hybrid Improper Ferroelectricity: A Mechanism for Controllable Polarization-Magnetization Coupling. *Physical Review Letters* **106**, 107204 (2011).
- Nowadnick, E. A. & Fennie, C. J. Domains and ferroelectric switching pathways in $\text{Ca}_3\text{Ti}_2\text{O}_7$ from first principles. *Physical Review B* **94**, 104105 (2016).
- Yoshida, Y. *et al.* Quasi-two-dimensional metallic ground state of $\text{Ca}_3\text{Ru}_2\text{O}_7$. *Physical Review B* **69**, 220411 (2004).
- Kikugawa, N., Rost, A. W., Hicks, C. W., Schofield, A. J. & Mackenzie, A. P. $\text{Ca}_3\text{Ru}_2\text{O}_7$: Density Wave Formation and Quantum Oscillations in the Hall Resistivity. *Journal of the Physical Society of Japan* **79**, 024704 (2010).
- Bohnenbuck, B. *et al.* Magnetic structure and orbital state of $\text{Ca}_3\text{Ru}_2\text{O}_7$ investigated by resonant x-ray diffraction. *Physical Review B* **77**, 224412 (2008).
- Bao, W., Mao, Z. Q., Qu, Z. & Lynn, J. W. Spin Valve Effect and Magnetoresistivity in Single Crystalline $\text{Ca}_3\text{Ru}_2\text{O}_7$. *Physical Review Letters* **100**, 247203 (2008).
- Sokolov, D. A. *et al.* Metamagnetic texture in a polar antiferromagnet. *Nature Physics* **15**, 671–677 (2019).

21. Nakatsuji, S., Ikeda, S.-I. & Maeno, Y. Ca_2RuO_4 : New Mott Insulators of Layered Ruthenate. *Journal of the Physical Society of Japan* **66**, 1868–1871 (1997).
22. Baumberger, F. *et al.* Nested Fermi Surface and Electronic Instability in $\text{Ca}_3\text{Ru}_2\text{O}_7$. *Physical Review Letters* **96**, 107601 (2006).
23. Horio, M. *et al.* Electron-driven C_2 -symmetric Dirac semimetal uncovered in $\text{Ca}_3\text{Ru}_2\text{O}_7$. *arXiv:1911.12163 [cond-mat]* (2019).
24. Tamai, A. *et al.* High-Resolution Photoemission on Sr_2RuO_4 Reveals Correlation-Enhanced Effective Spin-Orbit Coupling and Dominantly Local Self-Energies. *Physical Review X* **9**, 021048 (2019).
25. Acharya, S. *et al.* Evening out the spin and charge parity to increase T_c in unconventional superconductor Sr_2RuO_4 . *Communications Physics* **2**, 163 (2019).
26. Cao, G. *et al.* Observation of a metallic antiferromagnetic phase and metal to nonmetal transition in $\text{Ca}_3\text{Ru}_2\text{O}_7$. *Physical Review Letters* **78**, 1751 (1997).
27. Ohmichi, E. *et al.* Colossal magnetoresistance accompanying a structural transition in a highly two-dimensional metallic state of $\text{Ca}_3\text{Ru}_2\text{O}_7$. *Physical Review B* **70**, 104414 (2004).
28. Yoshida, Y., Ikeda, S.-I. & Shirakawa, N. Hall Effect in $\text{Ca}_3\text{Ru}_2\text{O}_7$. *Journal of the Physical Society of Japan* **76**, 085002 (2007).
29. Xing, H. *et al.* Existence of electron and hole pockets and partial gap opening in the correlated semimetal $\text{Ca}_3\text{Ru}_2\text{O}_7$. *Physical Review B* **97**, 041113 (2018).
30. Mousatov, C. H., Berg, E. & Hartnoll, S. A. Theory of the strange metal $\text{Sr}_3\text{Ru}_2\text{O}_7$. *Proc. Natl. Acad. Sci. U.S.A.* **117**, 2852–2857 (2020).
31. The relative spin orientation is reversed from bilayer to bilayer, due to the antiferromagnetic coupling between bilayers. Nonetheless, the inter-bilayer hopping is small, and so an effective ferromagnetic description is a good starting point for considering local interactions that can hybridise these states.
32. Bychkov, Y. A. & Rashba, E. I. Properties of a 2d electron gas with lifted spectral degeneracy. *JETP Letters* **39**, 78–81 (1984).
33. Zhang, X., Liu, Q., Luo, J.-W., Freeman, A. J. & Zunger, A. Hidden spin polarization in inversion-symmetric bulk crystals. *Nature Physics* **10**, 387–393 (2014).
34. Riley, J. M. *et al.* Direct observation of spin-polarized bulk bands in an inversion-symmetric semiconductor. *Nature Physics* **10**, 835–839 (2014).
35. Lee, J. S. *et al.* Pseudogap Dependence of the Optical Conductivity Spectra of $\text{Ca}_3\text{Ru}_2\text{O}_7$: A Possible Contribution of the Orbital Flip Excitation. *Physical Review Letters* **98**, 097403 (2007).
36. Warusawithana, M. P., Colla, E. V., Eckstein, J. N. & Weissman, M. B. Artificial Dielectric Superlattices with Broken Inversion Symmetry. *Physical Review Letters* **90**, 036802 (2003).
37. Sunko, V. *et al.* Maximal Rashba-like spin splitting via kinetic-energy-coupled inversion-symmetry breaking. *Nature* **549**, 492–496 (2017).
38. Caviglia, A. D. *et al.* Tunable Rashba Spin-Orbit Interaction at Oxide Interfaces. *Physical Review Letters* **104**, 126803 (2010).
39. Perry, R. & Maeno, Y. Systematic approach to the growth of high-quality single crystals of $\text{Sr}_3\text{Ru}_2\text{O}_7$. *Journal of Crystal Growth* **271**, 134–141 (2004).
40. Koepfner, K. & Eschrig, H. Full-potential nonorthogonal local-orbital minimum-basis band-structure scheme. *Physical Review B* **59**, 1743–1757 (1999).
41. Opahle, I., Koepfner, K. & Eschrig, H. Full-potential band-structure calculation of iron pyrite. *Physical Review B* **60**, 14035–14041 (1999). <http://www.fpllo.de>.
42. Perdew, J. P., Burke, K. & Ernzerhof, M. Generalized Gradient Approximation Made Simple. *Physical Review Letters* **77**, 3865–3868 (1996).
43. Blaha, P. *et al.* WIEN2k package, Version 10.1 (2010); available at, <http://www.wien2k.at>.

Supplementary Information for

Electronically driven spin-reorientation transition of the correlated polar metal $\text{Ca}_3\text{Ru}_2\text{O}_7$

I. Marković, M. D. Watson, O. J. Clark, F. Mazzola, E. Abarca Morales, C. A. Hooley, H. Rosner, C. M. Polley, T. Balasubramanian, S. Mukherjee, N. Kikugawa, D. A. Sokolov, A. P. Mackenzie, P. D. C. King

Phil D. C. King.

E-mail: philip.king@st-andrews.ac.uk

This PDF file includes:

Figs. S1 to S4

References for SI reference citations

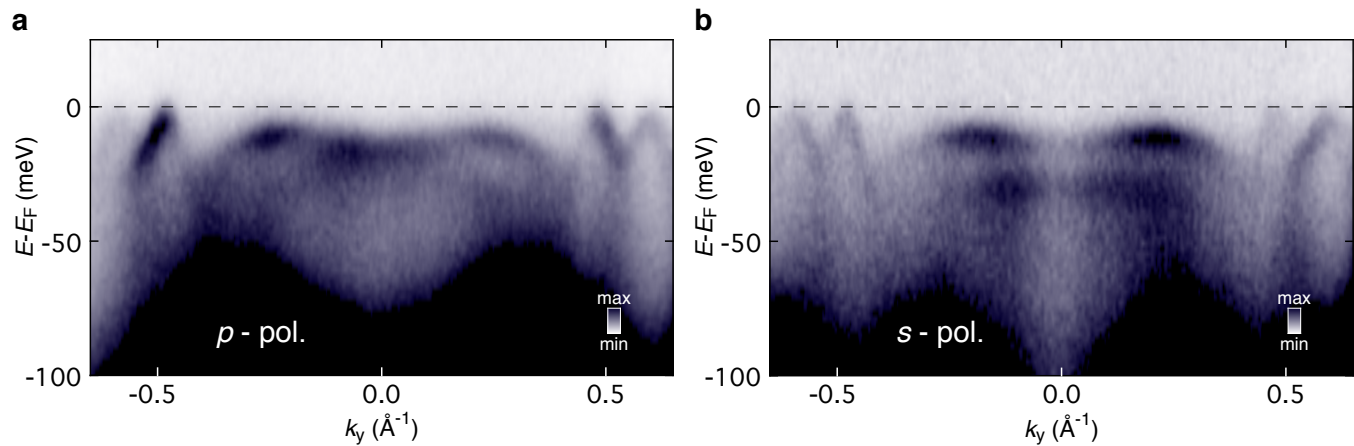


Fig. S1. Polarisation-dependent ARPES. Experimental dispersions measured along the Γ - M_y direction using (a) linear horizontal (p -) and (b) linear vertical (s -) polarised 22 eV synchrotron light at a sample temperature of 30 K. The photoemission transition matrix element modulates the observed photoemission intensity of the bands in momentum space based on the symmetry of the initial state orbitals, the polarisation vector of the incident light and the experimental geometry (1, 2). Using different orientations of the light polarisation vector we can therefore change the intensity of band features, which often thus yields a more complete picture of the measured band structure. In the data shown here, we can more clearly see both sides of the steep Λ -shaped bands close to the M_y zone edge using s -polarised light (see also inset of Fig. 1c of the main text), while the comparison between the two measurements clearly shows the multi-band structure of the flat, 'M-shaped' bands at the zone centre.

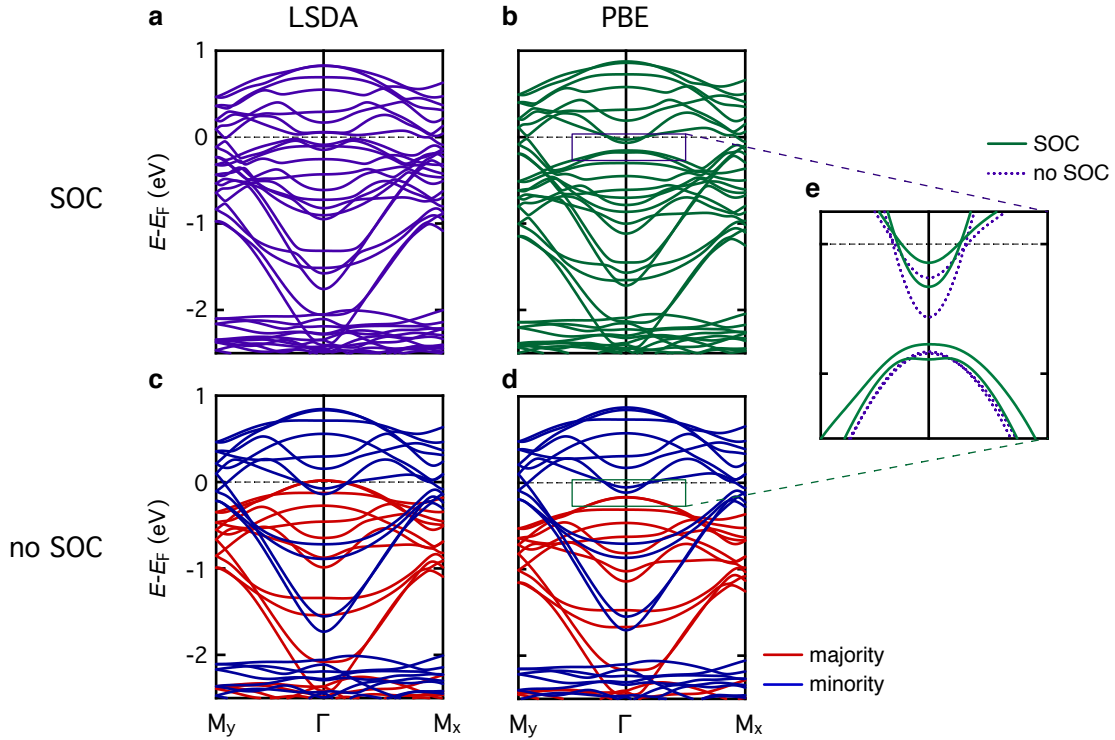


Fig. S2. Influence of exchange-correlation functional for DFT electronic structure. Electronic structure along M_y - Γ - M_x calculated assuming an FM- b magnetic order (i.e. magnetic moment orientated along b) and the experimental crystal structure at 8 K (3) using: (a,c) LSDA and (b,d) PBE functionals including (a,b) and excluding (c,d) spin-orbit coupling. As is often observed for generalised gradient (GGA) functionals vs. LDA ones, our PBE calculations exhibit a larger exchange splitting of the spin-majority (red) and spin-minority (blue) manifolds of Ru t_{2g} states than for the LDA calculations. This leads to the hole-like bands at Γ no longer intersecting the electron-like bands in the vicinity of the Fermi level. However, they are still close enough in energy such that spin-orbit coupling leads to a hybridisation, and consequent level repulsion, between the electron and hole bands for the FM- b configuration (e), which is not present for the FM- a or FM- c phases. We expect the experimental electronic structure to lie between the results for these two functionals, with the spin-majority hole-like and spin-minority electron-like bands close in energy, but potentially without significant band overlap. Our experimental measurements demonstrate that the hole bands at the zone centre in reality cross the Fermi level in the unhybridised state, and that the energy scale of the spin-orbit mediated band hybridisation is sufficient to push these states completely below the Fermi level. Since the experiments clearly show itinerant electrons at all temperatures, we refrain from using the Coulomb potential U in our calculations, which would lead to a large separation of states at Γ (4), and a significant change in dispersion inconsistent with the experimentally observed ‘M-shape’ states at the zone centre at temperatures below T_S .

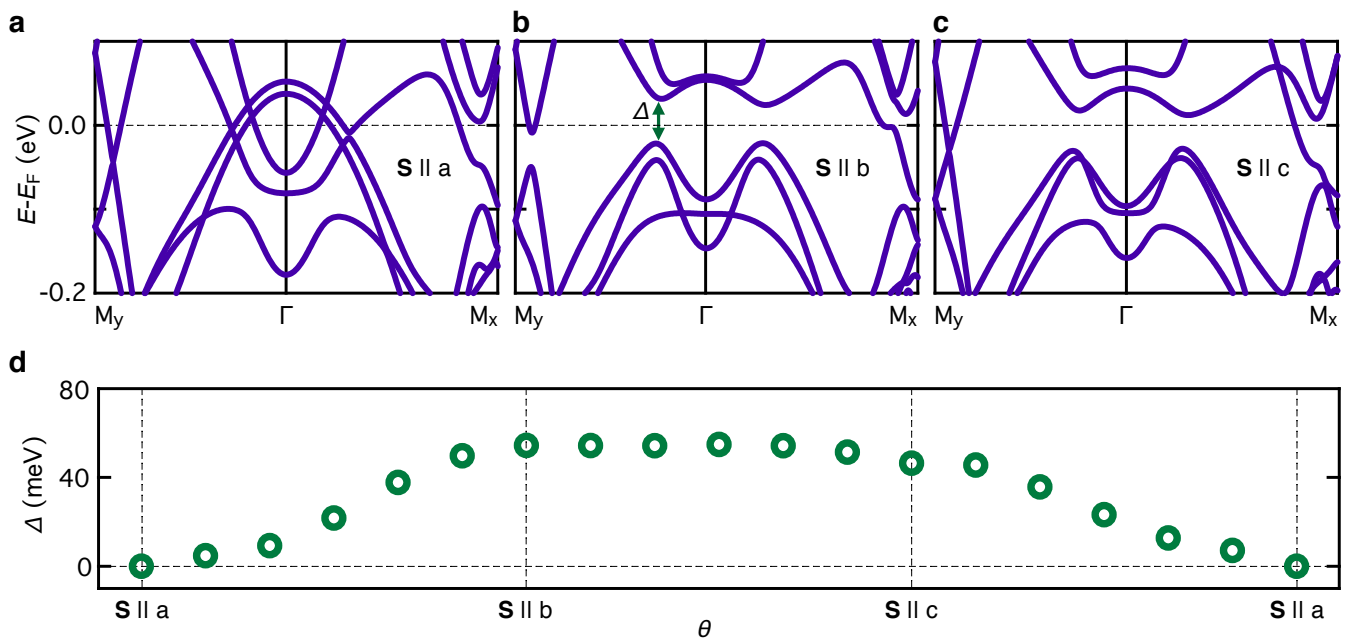


Fig. S3. Dependence of the Fermi surface hybridisation gap magnitude on magnetic moment orientation. (a-c) Calculated low-energy electronic structures along Γ - M_y and Γ - M_x , using LSDA+SOC calculations for the magnetic moment oriented along the (a) a , (b) b , and (c) c crystal axes. (d) Magnitude of the hybridisation gap which opens at the Fermi crossing along Γ - M_y , as the magnetic moment orientation is rotated by angle θ between the a - b - c - a axes. The gap opens gradually as the magnetic moment rotates away from the a -axis, but is almost invariant when the moment is rotated between the b and c axes.

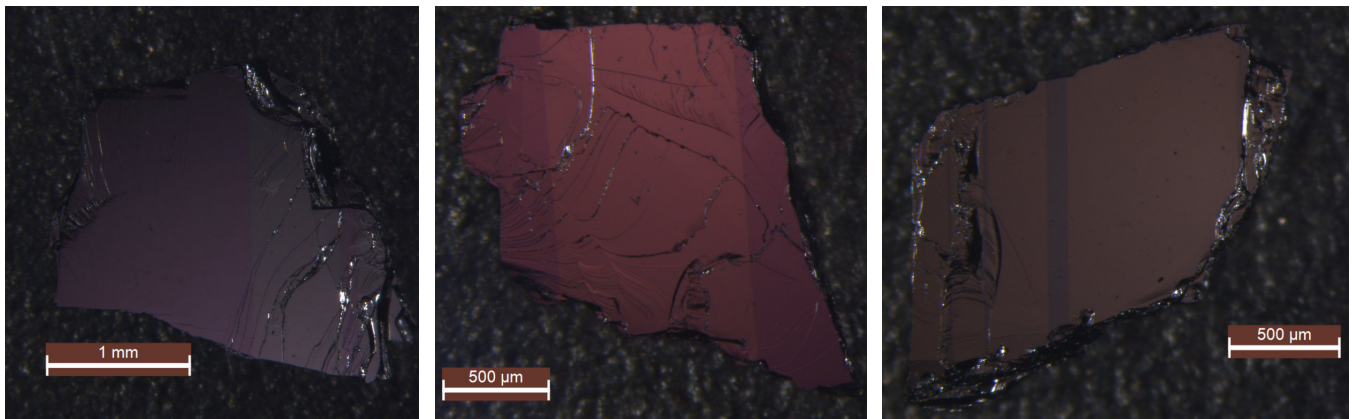


Fig. S4. Antiphase domains in $\text{Ca}_3\text{Ru}_2\text{O}_7$ single crystals. To prepare the single crystals of $\text{Ca}_3\text{Ru}_2\text{O}_7$ for ARPES measurements, we used polarised light optical microscopy (example measurements shown here), where the change in contrast indicates the presence of antiphase domains, i.e. switching of the a and b (short and long) in-plane crystal axes. The crystals were then cut to $\approx 500 \times 500 \mu\text{m}^2$ size from a single antiphase domain, before being mounted for ARPES measurements and cleaved *in situ*.

References

1. Damascelli, A. *et al.* Angle-resolved photoemission studies of the cuprate superconductors. *Review of Modern Physics* **75**, 473 (2003).
2. Day, R. P. *et al.* Computational framework chinook for angle-resolved photoemission spectroscopy. *npj Quantum Materials* **4**, 54 (2019).
3. Yoshida, Y. *et al.* Crystal and magnetic structure of $\text{Ca}_3\text{Ru}_2\text{O}_7$. *Physical Review B* **72**, 054412 (2005).
4. Liu, G.-Q. Mott transition and magnetic anisotropy in $\text{Ca}_3\text{Ru}_2\text{O}_7$. *Physical Review B* **84**, 235137 (2011).